Calculation of the global land surface energy, water and CO_2 fluxes with an off-line version of SiB2

C. Zhang,[1] D. A. Dazlich,[1] D. A. Randall,[1] P. J. Sellers,[2] and A. S. Denning[1]

Abstract. Global land surface fluxes of energy and CO_2 have been simulated using an off-line version of a biosphere-atmosphere model, SiB2, forced with analyzed or observed atmospheric boundary layer mean potential temperature, water vapor mixing ratio, and wind, surface downward solar and thermal radiation, and precipitation. The off-line model is called SiBDRV. Soil and vegetation boundary conditions were specified from satellite data and other sources. The European Centre for Medium-Range Weather Forecasts (ECMWF) data assimilation system products were used to derive the atmospheric and radiative forcings. Precipitation was based on station observations. The SiBDRV results were compared with corresponding simulation results produced by the Colorado State University general circulation model (CSU GCM), with the ECMWF assimilation system output and with observations. Differences between the surface energy budget components and the surface climatology produced by SiBDRV and the ECMWF assimilation system are due to differences in the land surface parameterizations between the two models. SiBDRV produced lower surface latent heat fluxes and larger sensible heat fluxes than the ECMWF data assimilation, partly due to large canopy resistent term explicitly formulated by SiB2 and possible precipitation differences between the SiBDRV precipitation forcing and the ECMWF data. Differences between the SiBDRV and the CSU GCM results are due to the different climates associated with the ECMWF assimilation system output, which is strongly constrained by assimilated observations, and by the CSU GCM, which is run in pure simulation mode. More specifically, the major reasons for the surface energy and CO_2 budget differences between the SiBDRV and the GCM are greater incoming solar radiation in the GCM and differences in the precipitation patterns. The simulated global annual carbon uptake by the terrestrial biosphere is similar in SiBDRV and the GCM. The annual gross primary productions of SiBDRV (116 Gt) and the GCM (113 Gt) agree well with other studies, using either ecological process models or empirical regression models. SiBDRV takes up 10 and 5% more CO_2 than the GCM in January and July, respectively. The seasonally varying land surface CO_2 fluxes estimated by the SiBDRV and the GCM both compare reasonably well with the results of other calculations.

1. Introduction

Land surface processes affect climate mainly through the surface-atmosphere exchanges of energy, momentum, and CO_2 across the atmospheric boundary layer. The land surface energy and CO_2 budgets are still uncertain, however, due to the complexity of the land surface processes and their interactions with the climate system. A comparison of 19 atmospheric general circulation models (GCMs) concluded that variations of the surface-energy fluxes in response to prescribed 4 K sea surface temperature changes varied greatly from model to model, mainly due to differences in the simulated hydrological cycles and the parameterizations of longwave radiation exchange, clouds, and boundary layer processes [*Randall et al.,* 1992]. These differences can arise in part from differences in the parameterization of land surface processes. The 19 models

used in the study mentioned above incorporated a wide range of parameterizations, from simple bucket models to relatively sophisticated vegetation parameterizations.

The biosphere-atmosphere transfer scheme (BATS) [*Dickinson,* 1984] and the simple biosphere model (SiB) [*Sellers et al.,* 1986] were developed to explicitly represent the effects of terrestrial vegetation and soil properties on surface-atmosphere fluxes. A new version of SiB (SiB2), described by *Sellers et al.* [1996a], includes more realistic canopy photosynthesis and stomatal control processes; vegetation transpiration is linked to carbon assimilation, and the rates of CO_2 exchange and water flux between the land surface and the atmosphere are calculated simultaneously. *Shao et al.* [1994] reviewed more land surface models involving intercomparison studies among the models.

Sato et al. [1989] published results from simulations using the first version of SiB (SiB1), as incorporated into the Center for Ocean-Land- and Atmosphere version of the U.S. National Meteorological Center's GCM. They showed that the surface fluxes of energy, momentum, heat, and moisture were in reasonable agreement with the available field observations.
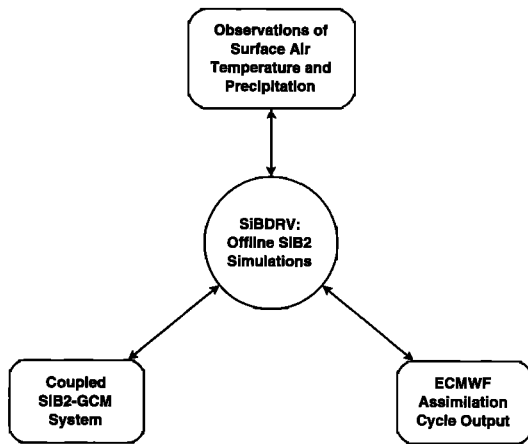
Recently, *Randall et al.* [1996] reported the results of simulations using SiB2 coupled to the Colorado State University

[1]Department of Atmospheric Science, Colorado State University, Fort Collins, Colorado.
[2]Laboratory for Atmospheres, NASA Goddard Space Flight Center, Greenbelt, Maryland.

Figure 1. Diagram illustrating the relationships among the simulations and data used in this study. SiBDRV is driven by a combination of European Centre for Medium-Range Weather Forecasts (ECMWF) analyses, ECMWF assimilation system output, and precipitation observations. The results produced by SiBDRV are compared with the ECMWF surface fluxes, with observations, and with simulations produced by the Colorado State University general circulation model (CSU GCM), which have the exactly the same SiB2 land surface model.

(CSU) GCM. Global data sets for the land surface biophysical parameters required by SiB2 were derived from satellite-observed normalized difference vegetation index (NDVI) data and global biome distributions, as described by *Sellers et al.* [1996b]. These simulations were compared with the results of a control simulation which used a bucket surface hydrology model having the same surface albedo and roughness length fields. Generally, SiB2 produces a warmer and drier surface and atmospheric boundary layer than the control run. The surface sensible heat flux increases and the surface moisture flux decreases, over the continents. The terrestrial carbon assimilation fields were also reasonably simulated using the coupled SiB2-GCM system. Compared with the control run, the coupled system produced less cloud cover over land and showed increases in the surface net shortwave radiation and longwave cooling, as well as less precipitation and more spatial variations of the soil wetness.

Pitman [1995] used a single-column model to study the sensitivity of BATS to variations of several input parameters. One of his conclusions is that such off-line test cannot fully evaluate land surface parameterizations because of the lack of surface-atmosphere feedbacks. We certainly agree with this, but at the same time, we find that tests of SiB2 inside a GCM are also somewhat unsatisfactory in themselves, because it is difficult to disentangle the problems that arise from deficiencies of SiB2 from those that arise from deficiencies of other parts of the GCM. One way to avoid this problem is to test SiB2 outside the GCM, by driving it with observations. Such a test is one of the main objectives of the present study. It seems to us that off-line tests and fully coupled tests are complementary and that both are desirable.

In this paper we report simulations of the global land surface energy and CO_2 fluxes, obtained by using an off-line version of SiB2, called "SiBDRV," which was forced ("DRiVen") by observed atmospheric and radiative forcings. The simulated surface energy and CO_2 budgets are compared with the results of simulations performed with the Colorado State University general circulation model (CSU GCM) coupled with exactly the same version of SiB2 and with the surface fluxes provided as part of the original ECMWF assimilation system output. The results are also compared with other available data sets. Figure 1 summarizes this strategy.

The differences between the land surface energy budget components and surface climatology produced by SiBDRV and the ECMWF assimilation system can be attributed to the differences between the land surface used in the two models. On the other hand, discrepancies between the SiBDRV results and the GCM simulation may be related to climatic differences experienced by the land surface.

This is a new attempt to reasonably estimate the land surface fluxes at the global scale, using a comprehensive land surface model (SiB2) forced by observations. Although some comprehensive field measurements for the surface energy and turbulent fluxes are now available at several locations, such as FIFE, HAPEX, Boreal Forest, surface energy fluxes at continental scale are not available at the present time. The surface fluxes also vary spatially. Thus a simulation such as SiBDRV can provide a practical way to obtain surface energy, water, and CO_2 fluxes information at the global scale and for a period of long time.

In section 2 we briefly describe SiB2. The boundary and atmospheric forcing data sets are discussed in section 3. Section 4 describes the experiments. In section 5 we analyze and discuss the results. A summary is given in section 6.

2. A Brief Description of SiB2

SiB2 includes one canopy layer. There are three soil layers: a surface soil layer, a root zone, and a deep soil layer. A canopy photosynthesis submodel [*Collatz et al.*, 1990, 1991, 1992; *Sellers et al.*, 1992] has been incorporated, with a prognostic stomatal conductance and an explicit calculation of the photosynthetic CO_2 flux between the atmosphere and the land surface. A new snow parameterization has also been included.

SiB2 has 10 prognostic variables: the vegetation canopy temperature (T_c), surface soil temperature (T_g), and deep soil temperature (T_d); water intercepted on the canopy $(M_{c,w})$ and on the surface soil layer (puddles, denoted by $M_{g,w}$); snow intercepted on the canopy $(M_{c,s})$ and on the surface soil layer $(M_{g,s})$; and surface soil wetness (W_1), root-zone soil wetness (W_2), and deep soil wetness (W_3).

Each of the three temperatures changes as a function of the surface energy fluxes. Following *Sellers et al.* [1996a], the sensible heat, moisture, and CO_2 fluxes are formulated in terms of their potential differences divided by aerodynamic resistances. Three components of evapotranspiration are included in SiB2: direct evaporation from intercepted water on the canopy and ground, transpiration of water vapor regulated by the stomatal conductance of the canopy, and evaporation from the surface soil layer. Temperatures for dry and wet surfaces are assumed to be the same.

The land surface albedo is determined by applying a two-stream radiative transfer model to the canopy layer [*Sellers et al.*, 1986]. Surface downward solar and thermal radiation are each partitioned into direct and diffuse visible (wavelength less than 0.72 μm), direct and diffuse near infrared (0.72–4.0 μm), and thermal infrared (wavelength greater than 4.0 μm) bands.

Photosynthesis is the source of biomass production over land and has been identified as one of the major CO_2 sinks for the atmosphere [e.g., *Schlesinger*, 1991]. As described by *Sellers et*

Table 1. List of Biomes As Defined and Used in SiB2

Biome Number	Biome Name
1	Broadleaf evergreen trees
2	Tall vegetation: broadleaf deciduous trees
3	Tall vegetation: broadleaf and needleleaf trees
4	Tall vegetation: needleleaf-evergreen trees
5	Tall vegetation: needleleaf-deciduous trees
6	Short vegetation/C4 grassland
7	Short vegetation: broadleaf shrubs with bare soil
8	Short vegetation: dwarf trees/shrubs
9	Agriculture/C3 grassland

al. [1992, 1996a], canopy photosynthesis is included in SiB2. The canopy carbon assimilation rate is regulated in three ways: rubisco limitation, light limitation, and transport limitation. The plant takes in CO_2 and releases water vapor through the leaf stomata. The stomatal conductance is expressed as a function of the net assimilation rate and the CO_2 concentration at the leaf surface, as discussed by *Collatz et al.* [1991 and 1992] and *Sellers et al.* [1992, 1996a]. Canopy transpiration of water vapor is thus directly related to canopy carbon assimilation through the canopy conductance. Transpiration in turn may feedback on the canopy conductance by affecting the canopy's environment.

The monthly CO_2 flux between the terrestrial biosphere and the atmosphere is estimated diagnostically as the difference between the monthly soil respiration $\bar{R}_{soil}$ and the net carbon assimilation rate, $\bar{A}_n$. Following *Randall et al.* [1996], the CO_2 flux is estimated as

$$\bar{F}_{CO_2} = \bar{R}_{soil} - \bar{A}_n, \tag{1}$$

where $\bar{R}_{soil}$ is calculated using

$$\bar{R}_{soil} = GPP \frac{\bar{R}_*}{\sum_{1year} (\bar{R}_* \Delta t)}, \tag{2}$$

$\bar{R}_*$ is the monthly mean soil respiration scale, which is a function of the layer-averaged soil temperature, root-zone soil moisture, and soil texture [*Randall et al.*, 1996]. The annual gross primary production (GPP) of the terrestrial biosphere is expressed as

$$GPP = \sum_{1year} \bar{A}_n(\Delta t), \tag{3}$$

In equations (1)–(3) we assume that the annual GPP is totally released by soil respiration, so that the annual mean CO_2 flux is zero at each location.

Nine vegetation types (biomes) are defined in SiB2, as listed in Table 1. The vegetation type for each grid cell is used to interpret satellite data to determine the values of parameters used in SiB2. These include the morphological properties of the canopy structure, the soil layer depths, canopy heights and leaf optical parameters, as well as physiological properties relating to canopy assimilation. These are generally not time-invariant quantities. Properties describing seasonal biosphere changes are derived for each biome based on the NDVI observations obtained through satellite remote sensing, including the fraction of incident photosynthetically active radiation (PAR) absorbed by the green canopy (FPAR), the canopy greenness, the leaf area index (LAI), and aerodynamic quantities, as shown by *Randall et al.* [1996] and *Sellers et al.* [1996b].

3. Forcing Data

The off-line SiB2 simulations need atmospheric forcing data, namely, the potential temperature, water vapor mixing ratio, and horizontal wind components in the atmospheric boundary layer; precipitation rate; and the downward solar and longwave radiation at the surface. The frequency of the input forcing data must be at least hourly in order to adequately resolve the diurnal cycle of the atmospheric physical processes and surface-atmosphere fluxes.

Table 2 lists the data sets and sources used for generation of the atmospheric forcing data. The data are all for the year 1987. They include (1) the daily total precipitation data observed through the global observation station network [*Shea et al.*, 1994]; (2) the monthly mean precipitation diurnal cycles as simulated with CSU GCM [*Randall et al.*, 1991]; and (3) six-hourly surface analyses and other assimilation system output obtained from the European Centre for Medium-Range Weather Forecasts (ECMWF).

The ECMWF assimilation system products were generated using operational cycle number 28, as described by *Blondin* [1988, 1991]. These products include surface temperature,

Table 2. List of Data Sources Used to Generate the Input Used in Off-Line SiB2 Simulations

Variable	Height	Frequency	Source
Zonal wind	10m	6 hourly	ECMWF
Meridional wind	10 m	6 hourly	ECMWF
Temperature	2 m	6 hourly	ECMWF
Dew point temperature	2 m	6 hourly	ECMWF
Friction velocity	surface	6 hourly	ECMWF
Sensible heat flux	surface	6 hourly	ECMWF
Latent heat flux	surface	6 hourly	ECMWF
Surface net shortwave radiation	surface	6 hourly	ECMWF
Surface net longwave radiation	surface	6 hourly	ECMWF
Surface albedo (snow free)	surface	6 hourly	ECMWF
Total cloud cover	N/A	6 hourly	ECMWF
Vegetation cover	surface	monthly	*Sellers et al.* [1996b]
Total precipitation rate	surface	daily	*Shea et al.* [1994]
Diurnal cycle of the precipitation rate	surface	monthly	CSU GCM output

The ECMWF surface fluxes are also used for comparison with the SiBDRV results.

Surface Air Temperature (K)

DJF   JJA
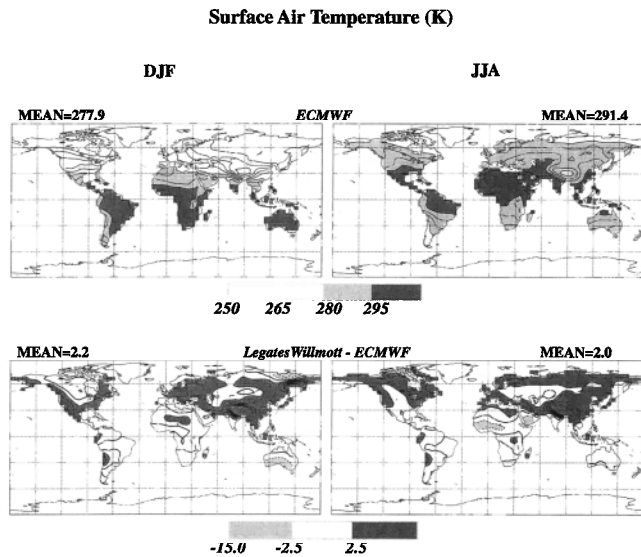
Figure 2. Comparisons of the 2-m ECMWF surface air temperature with surface air temperature climatology of *Legates and Willmott* [1990a] for December, January, and February (DJF) and June, July, and August (JJA). The contour interval is 5.0 K in the top panel and 2.5 K in the bottom panel.

moisture, winds, and surface energy fluxes on a six-hourly basis. Three soil layers were considered but without explicit vegetation. The two prognostic temperatures and two soil wetnesses for the top two layers were based on derivations of *Budyko* [1956] and *Deardorff* [1978]. The deepest layer temperature and soil wetness were assigned fixed "climatological" values. The surface sensible and latent heat fluxes were parameterized, using the bulk formulas of *Louis* [1979] and *Louis et al.* [1982]. These products were produced as the ECMWF model was run in an operational data assimilation mode, in which observed winds, temperatures, and humidities, and other data were inserted every 6 hours. In effect the model interpolates the observations in space and time, providing a dynamically consistent representation of the state of the atmosphere. It is important to recognize, however, that the results produced in this way are not pure observations because the formulation of the model does affect the results. Nevertheless, the ECMWF assimilation system products for the winds, temperature, and humidity are strongly constrained by the assimilated observations where the data density is high enough.

As discussed below, we also use certain other ECMWF assimilation system products, including for example the surface solar radiation. This most assuredly is not an observation, although the values obtained have been influenced by observations, e.g., of humidity. The surface sensible and latent heat fluxes produced by the ECMWF assimilation system are also used here, not as input to SiBDRV but rather for comparison with results produced by SiBDRV. While these ECMWF surface sensible and latent heat flux products are not observations, they have been influenced by the assimilated observations of the winds, temperature, and humidity. We refer to these and similar ECMWF model-generated fields as "ECMWF assimilation system output."

3.1. Atmospheric Boundary Layer Data

The surface transfer parameterization used in SiBDRV (and the CSU GCM), which is based on the work of *Deardorff*

[1972], accepts as input "mixed layer" values of the potential temperature (Θ_m), water vapor mixing ratio (q_m), and the horizontal wind components u_m and v_m. During the day these values are characteristic of the well-mixed layer that is typically observed to fill the upper portion of the atmospheric boundary layer. At night these values are interpreted as being representative of the upper portion of the typically stable and relatively shallow nocturnal boundary layer.

To generate suitable values for use with SiBDRV, the ECMWF 2-m surface temperature (T_{2m}), 2-m dew point temperature (T_{2dew}), and 10-m surface winds $(u_{10}$ and $v_{10})$ were extrapolated up to a height of 50 m above the land surface, which we assume is a representative depth of the lower part of the mixed layer in the sense defined above. Surface similarity flux-profile relations [*Paulson*, 1970; *Businger et al.*, 1971] were used to generate these values based on the surface turbulent fluxes of momentum, heat and moisture, and surface pressure from the ECMWF assimilation system together with the SiB2 surface roughness length and displacement height. We are aware that surface similarity theory may not work well for very rough and heterogenous surfaces [*Garratt*, 1977]. The error becomes small, however, above twice the canopy height. The six-hourly mixed layer values were further interpolated to obtain hourly values, with the aid of a cubic spline method [*Burden and Faires*, 1985].

Figure 2 compares the 2-meter air temperature from the ECMWF assimilation system, T_{2m}, with the climatology of *Legates and Willmott* [1990a]. The temperatures from the ECMWF assimilation system are generally cooler than those of Legates and Willmott, with global mean differences of 2.2 and 2.0 K in winter and summer, respectively. In regions such as eastern Siberia, the northern boreal forests, East Asia, and the East and West Coasts of North America, there are larger temperature differences (more than 4 K). This is consistent with the discussion of *Blondin* [1988], who showed that the version of the ECMWF model used to produce the assimilation products employed here overestimated surface evaporation, and so produced excessively cool surface temperatures, particularly in the northern hemisphere.

The surface transfer parameterization of *Deardorff* [1972] requires as input the depth of the atmospheric boundary layer. For the SiBDRV simulations this depth was set to 50 mbar. In the GCM and SiBDRV simulations the surface-boundary transfer coefficients are calculated diagnostically as functions of the bulk Richardson number.

3.2. Surface Radiation Forcing

SiBDRV uses the SiB2 surface albedo prescription. Nevertheless, the land surface albedos produced by the ECMWF assimilation system are needed for the calculation of the downward surface shortwave radiation flux, which was not available in the ECMWF assimilation system output. The albedos were estimated using

$$\alpha_{sfc} = \left(1 - \frac{a \cdot M_{gs}}{Z_m}\right) \cdot \alpha_{soil} + \left(\frac{a \cdot M_{gs}}{Z_m}\right) \alpha_{snow} \qquad (4)$$

for forested regions, and

$$\alpha_{sfc} = (1 - A_{snow}) \cdot \alpha_{soil} + A_{snow} \cdot \alpha_{snow} \qquad (5)$$

for bare soil or short grass cover. In (4), α_{soil}, α_{snow}, and M_{gs} are the snow-free background soil albedo, the snow albedo, and the snow water mass per unit area, respectively, and Z_m is

the effective snow-masking depth. Our methods to determine Z_m and α_{snow} are discussed in the Appendix.

Estimates of the downward surface solar radiation fluxes were first derived from the snow-free land surface albedo α_{soil}, by combining the ECMWF assimilation system output and the net surface solar radiation, using *Goudriaan's* [1977] method to decompose the total solar radiation into visible (S^v) and near-infrared (S^n) components. An iteration was used to compute the land surface albedo, given the snow-free surface albedo, total surface net solar radiation, snow, and cloud cover.

Figure 3 shows the estimated mean surface albedo α_{sfc} for December, January, February (DJF), and June, July, and August (JJA), as well as the differences between the ERBE (Earth Radiation Budget Experiment) [*Barkstrom*, 1984] clear-sky albedo and the estimated surface albedo. The estimated ECMWF land surface albedo is in good agreement with the ERBE clear-sky albedo, although, of course, they are not expected to be the same because the ERBE clear-sky albedo includes the effects of Rayleigh scattering by the gaseous atmosphere. The seasonal global mean differences are 3.8 and 2.8% for winter and summer, respectively. There are larger differences at higher latitudes and over snow/ice covered land, in part because ERBE is generally unable to identify clouds over snow and ice surfaces.
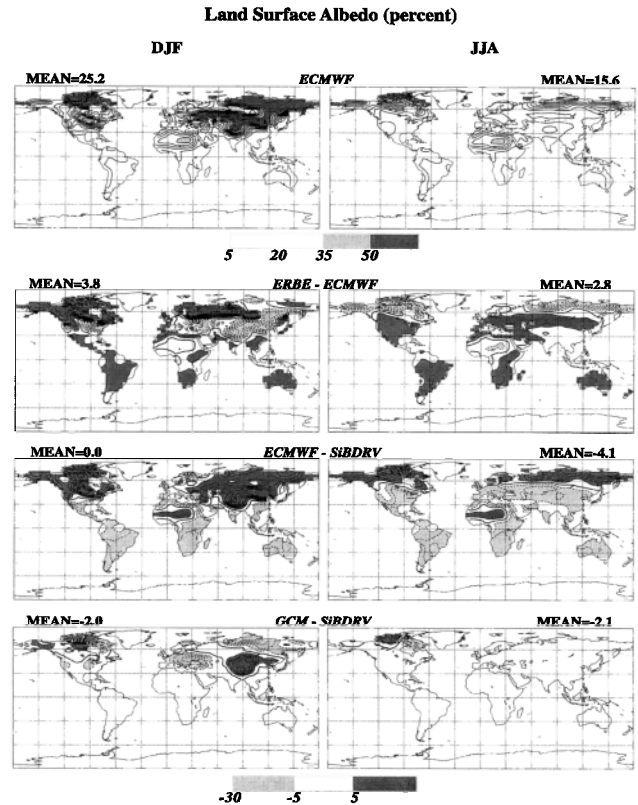
The SiBDRV-simulated land surface albedos are compared with the ECMWF values, and with the GCM (Figure 3). There are large surface albedo differences between ECMWF and SiBDRV. In the northern winter the surface albedo used in the ECMWF assimilation system is about 5 to 25% higher than the SiBDRV albedo over the northern hemisphere but is lower than the SiBDRV albedo in the southern hemisphere. During the northern summer, ECMWF has higher land surface albedos in the northern boreal forest regions and near the Arctic Circle and lower surface albedos in the midlatitudes and over much of the southern hemisphere. This is due to differences in the treatment of snow-free soil/vegetation albedo between the ECMWF assimilation system and the SiB2. The snow-free soil albedos from the ECMWF system are set as constants for each land point, without consideration of seasonal vegetation changes, while SiB2 does consider the seasonal vegetation changes. For the Sahara desert, the ECMWF assimilation system used a higher surface albedo than SiB2; SiB2 prescribes the desert albedos following the ERBE clear-sky albedo [*Sellers et al.*, 1996b]. The SiBDRV surface albedos for snow-free surfaces agree well with the values obtained in the GCM simulation for the summer months (Figure 3); on this basis we believe that the radiation components have been adequately approximated by the empirical formula.

The surface downward solar radiation was calculated from the surface albedo and surface net solar radiation flux. The hourly surface downward solar radiation flux, SWD(t), was interpolated from the six-hourly data using

$$\text{SWD}(t) = \text{SDT} \cdot \Phi(t), \qquad (6)$$

where SDT is total accumulated solar energy during the day and $\Phi(t)$ is a weighting function, given by

$$\Phi(t) = \frac{[1 - C(t)] \cdot \sin\left(\dfrac{\pi t}{DL}\right)}{\displaystyle\sum_{t=sr}^{ss} [1 - C(t)] \cdot \sin\left(\dfrac{\pi t}{DL}\right)}. \qquad (7)$$

Land Surface Albedo (percent)

Figure 3. The land surface albedo used by ECMWF and comparisons with the ERBE clear-sky albedo for DJF and JJA, and comparisons of the SiBDRV surface albedo with the ECMWF values and with the GCM, for DJF and JJA. The contour interval is 5% in all panels.

In (7), $C(t)$ is the total cloud cover (fraction), DL is daylight length (hours), and SS and SR are the times of sunset and sunrise, respectively.

The surface downward thermal radiation flux (LWD) was computed from the net surface longwave radiation flux (LWN) and the ground surface temperature (T_g), using LWD = LWN + $\varepsilon \sigma T_g^4$. We have assumed that the surface emissivity ε is 1.0 for all types of land surface. A cubic spline method was used to interpolate the six-hourly downward radiation data into an hourly data set.
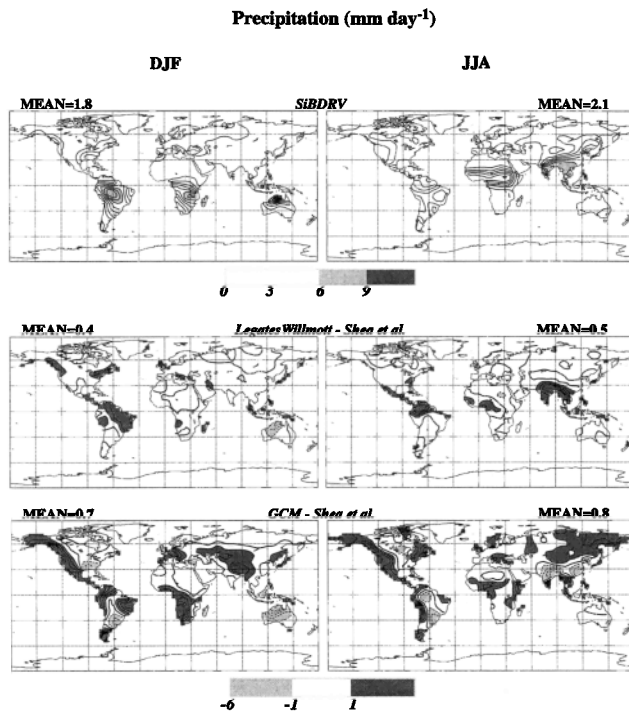
3.3. Precipitation

The observed daily total precipitation data set for 1987 [*Shea et al.*, 1994] was used to generate the hourly precipitation data, aided by the GCM-simulated monthly mean diurnal cycle. The interpolation was done using

$$P_T(t) = P_d \chi(t), \qquad (8)$$

$$\chi(t) = P_{dcl}(t) \bigg/ \left(\sum_{t=0}^{23} P_{dcl}(t) \right), \qquad (9)$$

where P_d is daily total precipitation, P_{dcl} is the monthly mean diurnal cycle (first and second diurnal harmonics only) of the precipitation, as simulated by the CSU GCM [*Randall et al.*, 1991], and $P_T(t)$ is the hourly interpolated precipitation rate. Negative values of P_{dcl} were set to zero.

Figure 4 shows a comparison of the precipitation rate used as input to SiBDRV, as described above, and the precipitation

Precipitation (mm day⁻¹)

DJF   JJA

Figure 4. The input precipitation observations as derived from the data of *Shea et al.* [1994] (top) and comparisons with the precipitation climatology of *Legates and Willmott* [1990b] (middle) and with the GCM-simulated precipitation [*Randall et al.*, 1996] (bottom) for DJF and JJA. The contour interval is 1.0 mm d⁻¹ in all panels.

climatology of *Legates and Willmott* [1990b], for December, January, and February (DJF) and June, July, and August (JJA). The SiBDRV precipitation is in fair agreement with the precipitation climatology, although the climatological global means over land are about 0.37 and 0.49 mm d⁻¹ greater in winter and summer, respectively. The largest differences are in the tropics, particularly in India and Southeast Asia, where the SiBDRV values are generally less than the climatology. It should be noted that we are comparing precipitation from a particular year with a multiyear climatology; the differences may thus be due to interannual variations. The SiBDRV precipitation was not corrected for rain gauge errors, as was done by *Legates and Willmott* [1990b], and we expect generally to underestimate the precipitation without such corrections.

Finally, the total precipitation rate was arbitrarily divided equally into convective and stratiform precipitation. This partitioning is needed for the surface runoff and infiltration computations in SiB2 [*Sellers et al.*, 1996a].

3.4. Coupling of SiB2 and Forcing Data

The surface downward solar and longwave radiation fluxes, precipitation rate, and the atmospheric boundary layer's wind, temperature, and mixing ratio are provided hourly to SiB2. As the model runs, the forcing variables are interpolated linearly for each integration step of 6 min.

4. Experimental Design

The six-hourly ECMWF assimilation system output provided to us started from 0000 GMT on January 1, 1987, and ended at 2400 GMT on December 31, 1987. The data were at

2.5 × 2.5° grid resolution and were regridded to 4 × 5°, which is the resolution used in this study.

Exactly the same land surface parameterization (SiB2) was used in SiBDRV and in the GCM simulation. The biophysical and soil parameters of the land surface boundary conditions were based upon the 1987 NDVI data and global biome distributions. Thus the input atmospheric forcings and the land surface parameters are consistent with each other.

SiBDRV was initialized using a state from an earlier GCM simulation with SiB2. SiBDRV was then integrated for five simulated years, with repeating 1987 conditions. The first four simulated years were used to allow SiBDRV to equilibrate to the prescribed forcing. The fifth and last simulated year is analyzed here. Although the GCM was run for 10 years (from 1978 to 1988), only the data from 1987 are compared with the SiBDRV results.

5. Results

5.1. Surface Air Temperature and Water Vapor Mixing Ratio

Figure 5 shows the DJF and JJA seasonal mean surface air temperatures (T_a) as simulated by SiBDRV, as well as comparisons of SiBDRV results with the 2-meter surface air temperatures (T_{2m}) from the ECMWF assimilation system output

Surface Air Temperature (K)

DJF   JJA
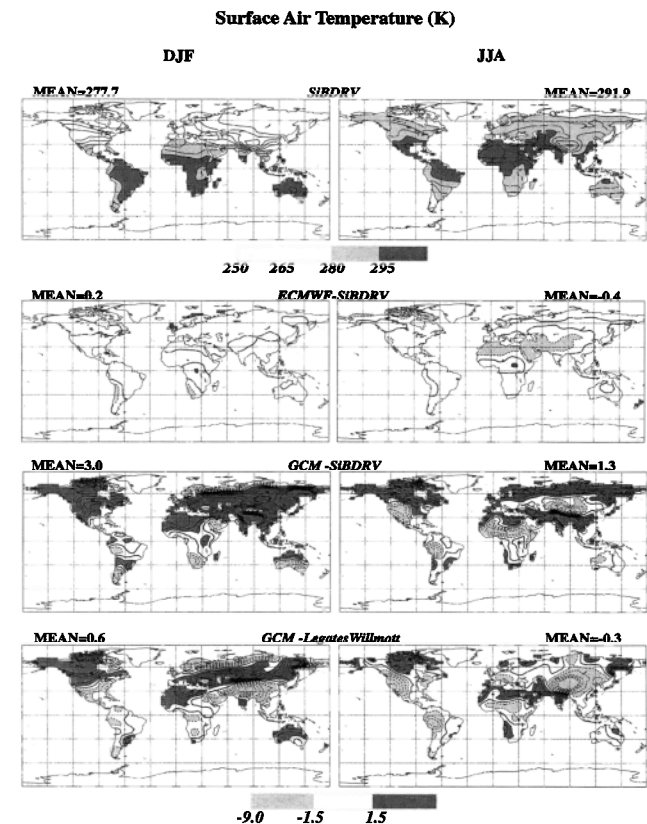
Figure 5. SiBDRV-simulated surface air temperature (top panel) and comparisons of SiBDRV with the 2-m ECMWF surface air temperature (second panel) and with the GCM simulated surface air temperature (third panel), for DJF and JJA. A comparison of the GCM results with the surface air temperature climatology of *Legates and Willmott* [1990a] for DJF and JJA are shown in the bottom panel. The contour interval is 5.0 K in the top panel and 1.5 K in other panels.

and with the GCM-simulated surface air temperatures. The surface air temperature and humidity in both SiBDRV and the GCM simulations are representative of the air in the canopy and are diagnostically computed from the corresponding surface and mixed layer values.

The T_a obtained with SiBDRV agrees well with T_{2m} from the ECMWF assimilation system output over much of the global continents, for both DJF and JJA. The SiBDRV climate is slightly warmer than the climate produced by the ECMWF assimilation system in the midlatitude deserts for JJA and in the deserts in the southern hemisphere for DJF.

The GCM simulation gives much warmer T_a than does SiBDRV over much of the global continents, especially over the northern hemisphere in DJF. The seasonal global mean T_a differences are 3.0 and 1.3 K in DJF and JJA, respectively. The larger T_a differences in DJF are due to less snow cover in the GCM simulation (discussed later), where temperature differences are about 10 K warmer. In JJA, the T_a differences are more likely affected by the surface solar radiation which is related to cloud effects, as discussed later.

Figure 5 also compares surface air temperatures of the GCM with the observations in DJF and JJA. The global mean temperatures of the GCM are much closer to the observations, with global mean temperature differences of 0.6 and −0.3 K in DJF and JJA, respectively. However, the GCM is warmer than observed over the northern hemisphere in DJF and cooler than observed over much of the northern hemisphere in JJA. Figure 4 shows that the GCM generally produces more precipitation in the regions that the model makes cooler than observed.

Figure 6 shows the seasonal mean surface air water vapor mixing ratio (q_a) as simulated by SiBDRV, and a comparison with the 2-m mixing ratio from the ECMWF assimilation system (q_{2m}), and with the simulated surface water vapor mixing ratio in the GCM. The seasonally varying global mean values are close among the simulations and the ECMWF assimilation system output, although the mixing ratio differences show slightly moister surface air in SiBDRV than in the GCM or the ECMWF assimilation system output. More specifically, SiBDRV has moister surface air in the southern hemisphere in DJF and is generally moister in the subtropical regions in the northern hemisphere in JJA. The q_a differences between the GCM and the SiBDRV simulations are mainly located in the southern hemisphere and the subtropics in DJF and in the Amazon, North America, India, Southeast Asia, and desert regions during JJA, where precipitation differences (Figure 4) are very well correlated with the q_a differences.

5.2. Solar and Terrestrial Radiation

Figure 7 shows the surface net solar radiation fluxes produced by SiBDRV, and comparisons with ECMWF, with the CSU GCM, and with the retrievals of Li and Garand [1994] for winter and summer. The observed all-sky surface net shortwave radiation [Li and Garand, 1994] was derived from the ERBE clear-sky solar radiation at the top of the atmosphere and the ECMWF total precipitable water data, using an empirical radiative transfer parameterization.

In the seasonal global mean, SiBDRV absorbs 6.4 and 7.9 W m^{-2} less solar radiation on land than does ECMWF, for DJF and JJA, respectively. The mean differences between the GCM and the SiBDRV, however, show that the GCM absorbs 18.7 and 8.1 W m^{-2} more net shortwave radiation flux on the land surface in DJF and JJA, respectively. The SiBDRV incident

Surface Water Vapor Mixing Ratio (g kg⁻¹)
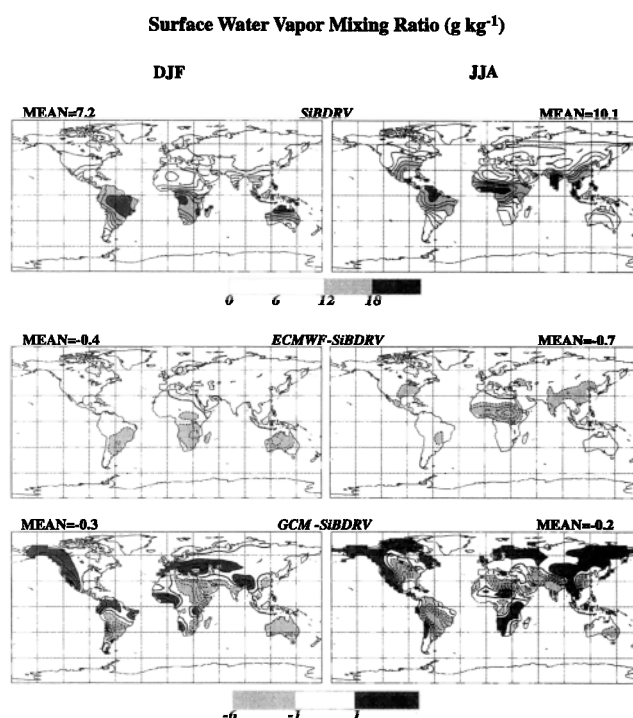
Figure 6. SiBDRV-simulated surface air water vapor mixing ratio (top) and comparisons of SiBDRV with the 2-m water vapor mixing ratio from the ECMWF assimilation system output (middle) and with the GCM-simulated surface air water vapor mixing ratio (bottom), for DJF and JJA. The contour interval is 2.0 g kg^{-1} in the top panel and 1.0 g kg^{-1} in the bottom two panels.

global surface shortwave radiation is about 4.0 W m^{-2} (3.4%) and 9.0 W m^{-2} (4.6%) more than the Moats et al. [1994] all-sky surface shortwave radiation for DJF and JJA, respectively.

SiBDRV tends to absorb less surface net shortwave radiation than ECMWF in South America and Australia but more in the northern hemisphere land regions in winter. During summer, the middle- and high-latitude regions of the northern hemisphere and much of the southern hemisphere land absorb less surface net shortwave radiation in SiBDRV than the ECMWF assimilation system, but for the Sahara desert and at high latitudes of the northern hemisphere, SiBDRV absorbs more solar radiation than ECMWF.

Snow cover differences, shown in Figure 8, produce large albedo differences between the ECMWF assimilation system output and the SiBDRV simulation in winter (Figure 3). Over the Eurasian boreal forests in high latitudes, there is more snow in SiBDRV than in the ECMWF assimilation system output, but nevertheless SiBDRV gives a lower surface albedo, because the ECMWF assimilation system includes less of a vegetation masking effect and uses a higher albedo for the snow-free soil. The snow cover produced by the ECMWF assimilation system was based on values calculated from surface air temperature and precipitation, except for parts of Canada and Europe where snow cover was observed at stations, area averaged, and interpolated [European Center for Medium-Range Weather Forecasts (ECMWF), 1987]. The maximum snow depth was limited to 140 cm in Canada and Europe. Unfortunately, the precipitation produced by the ECMWF assimilation system was not available for this study.

Comparisons between the SiBDRV and the GCM (Figure 8)

Surface Net Solar Radiation (W m⁻²)
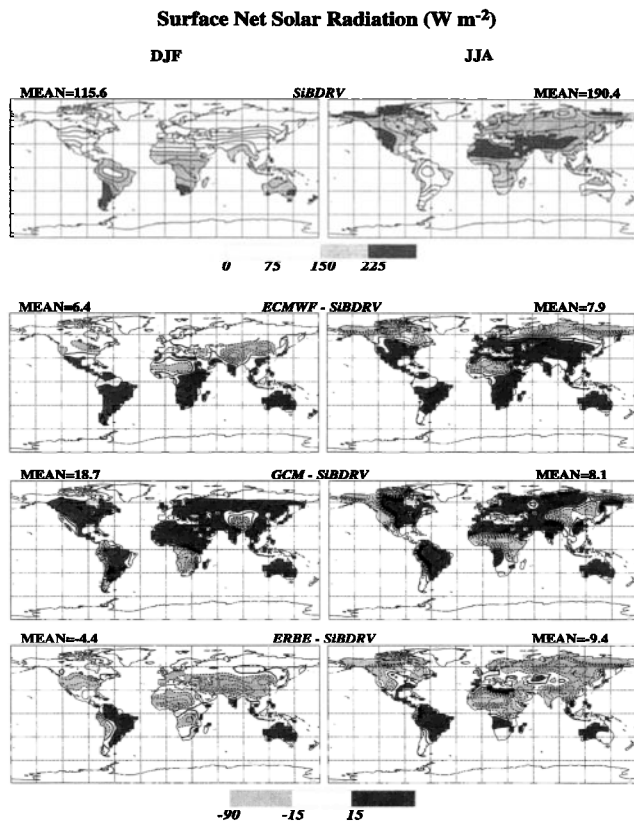
Figure 7. Surface net solar radiation fluxes as produced by SiBDRV (top) and comparisons of the SiBDRV results with the ECMWF assimilation system output (second panel) and with the GCM (third panel). A comparison between SiBDRV and retrievals of surface net solar radiation fluxes by *Li and Garand* [1994], based on Earth Radiation Budget Experiment (ERBE) data, are shown in the bottom panel. The contour interval is 25 W m⁻² in the top panel and 15 W m⁻² in the other panels.

show that in DJF the continents absorb more shortwave radiation in the GCM than in the SiBDRV, except on the east coasts of South America, South Africa, and the Tibetan plateau. During the northern summer, SiBDRV absorbs more shortwave radiation in western North America, the west coast of South America, eastern Asian continent, and the southern Sahara region. The snow cover differences, as shown in Figure 8, only partially explain the higher surface albedo and the smaller surface net solar radiation produced by SiBDRV in the northern hemisphere in winter. There is little surface albedo difference between the SiBDRV and the GCM (Figure 3) in the summer, except at very high latitudes, where SiBDRV shows a higher surface albedo because of persistent snow cover.

The relatively large amount of absorbed surface solar radiation in the GCM, shown in Figure 8, is due to excessive downward surface solar radiation. The clouds used for SiBDRV (from the ECMWF assimilation system output) were compared with the total cloud cover as simulated by the GCM (not shown). We found there was more cloud cover in the GCM than in the ECMWF assimilation system output. The seasonal global mean cloud differences were large: 24 and 30% in DJF and JJA, respectively. This seems in conflict with the fact that there is generally more surface net solar radiation flux

over much of the land area in the GCM (Figure 8). The explanation is that the GCM clouds are optically thinner than the clouds produced by the ECMWF assimilation system. The global mean total cloud covers produced by the ECMWF assimilation system are 53 and 44% over land for DJF and JJA, respectively. The cloud cover produced by the ECMWF assimilation system agrees much better with the International Satellite Cloud Climatology Project (ISCCP) data. On the other hand, the GCM had 29 and 25% more total cloud cover than shown by the ISCCP data set, for DJF and JJA, respectively.

Excessive surface net solar radiation in the GCM tends to increase the surface temperature and the turbulent fluxes of sensible and latent heat, as well as the longwave radiative cooling of the surface. The surface net longwave radiation is also affected by cloud cover, atmospheric water vapor and temperature, through the downward component of the longwave radiation. Figure 9 shows the surface net longwave radiation in SiBDRV (negative contours show surface cooling), and a comparison with the ECMWF assimilation system output, and with the GCM simulation. The GCM generally produces more surface longwave cooling than SiBDRV in the northern hemisphere in both DJF and JJA, because of the warmer land surface in the GCM. On the West Coast of North America and over the tropical and southern hemisphere continents, there is more surface longwave cooling in SiBDRV, because there is less cloud and a relative warmer and drier land surface in those regions.

There are differences in precipitation between the SiBDRV and the GCM (Figure 4). Of course, precipitation is correlated with cloud cover to some extent, so that cloudy regions have less incoming surface solar radiation and a cool and moist land
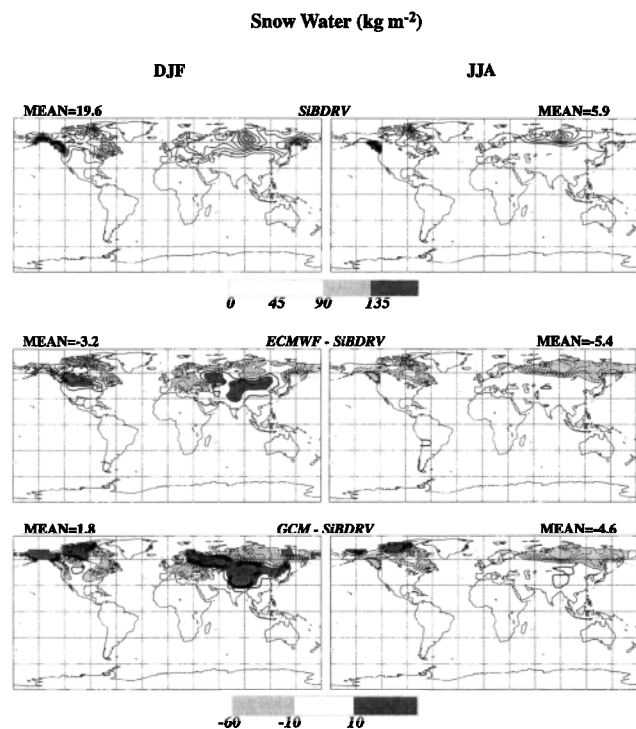
Snow Water (kg m⁻²)

Figure 8. SiBDRV-simulated snow water equivalent (top) and comparisons with the ECMWF assimilation system output (middle) and with the GCM simulations (bottom), for DJF and JJA. The contour interval is 15 kg m⁻² in the top panel and 10 kg m⁻² in the bottom two panels.

surface. A more recent version of the GCM includes a new stratiform cloudiness parameterization [*Fowler et al.*, 1995] and the GCM-simulated precipitation distributions are in much better agreement with observations.

The surface net longwave radiation fluxes agree well between the ECMWF assimilation system and the SiBDRV, as shown in Figure 9, although SiBDRV produces slightly more surface net longwave cooling than the ECMWF assimilation system in the southern hemisphere during DJF, and in the midlatitude desert regions of the northern hemisphere during JJA. The land surface temperature affects the upward surface longwave radiation. In the ECMWF assimilation system the soil heat capacity is set to a constant 2.4×10^6 J m^{-2} K^{-1}. In SiB2, however, the soil heat capacity is calculated as a function of soil moisture such as discussed by *Sellers et al.* [1996a] and is affected by precipitation and snow accumulation/melting. Over deserts and other dry regions, SiBDRV tends to have warmer ground and more surface longwave cooling than the ECMWF assimilation system. In far eastern Siberia, SiBDRV produces less surface cooling due to more snow on the ground in JJA (Figure 8).

5.3. Sensible and Latent Heat Fluxes

Figure 10 shows the land surface sensible heat flux simulated by SiBDRV and comparisons with the GCM simulation and the ECMWF assimilation system output. The surface sensible heat flux differences between SiBDRV and the ECMWF assimilation system output (Figure 10) depend very much on location. In winter, SiBDRV produces less sensible heat flux over much of the globe but more in North America and Asia. In summer, SiBDRV tends to produce a larger sensible heat
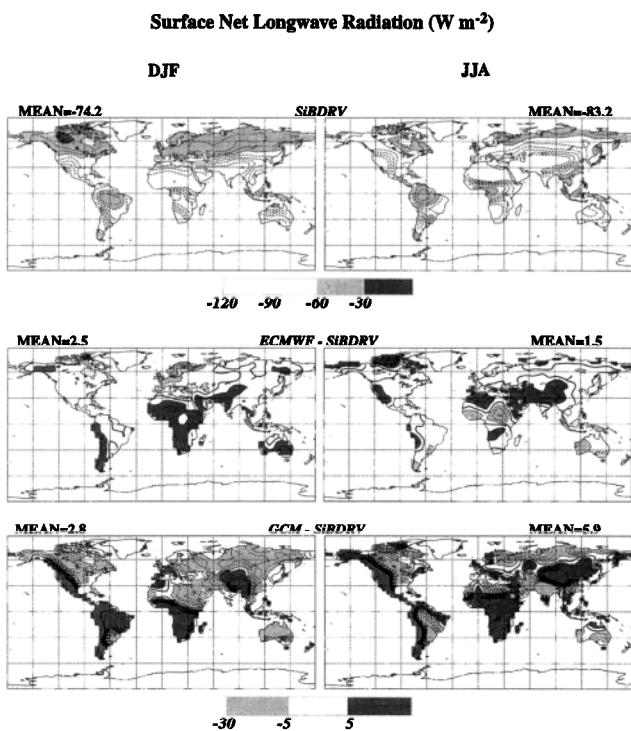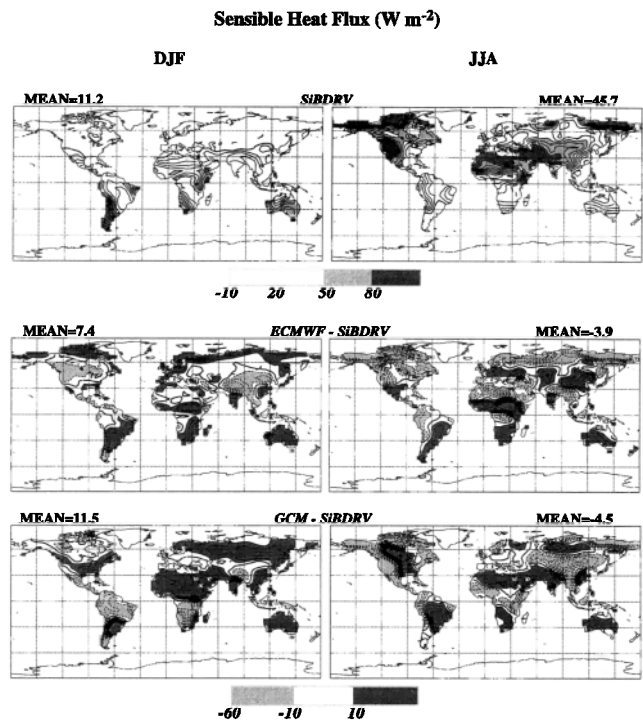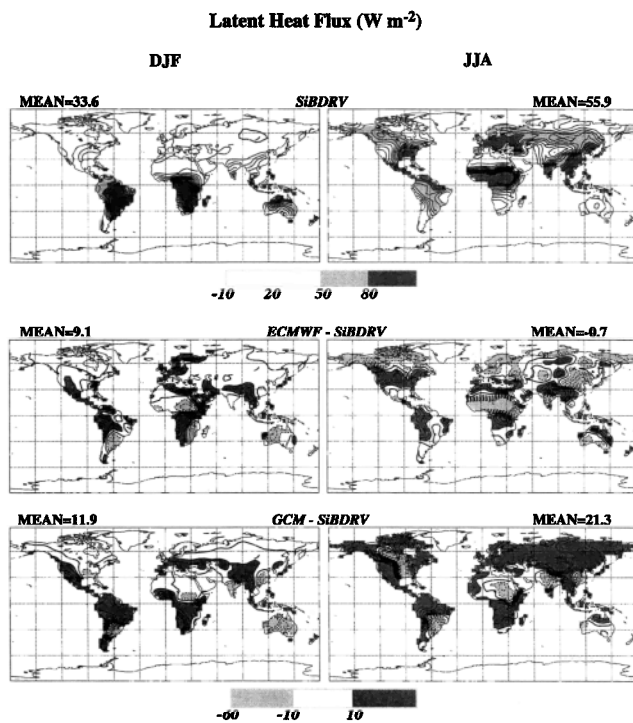

Figure 10. Surface sensible heat flux of SiBDRV (top) and comparisons with the ECMWF assimilation system output (middle) and with the GCM simulations (bottom), for DJF and JJA. The contour interval is 10 W m^{-2} in all panels.

flux over land, especially over North America, North Africa, and at high latitudes of Eurasia. More sensible heat flux is produced in the GCM than SiBDRV (Figure 10), over much of the globe in winter, except in the Amazon and southern Africa. In summer the GCM produces a much larger sensible heat flux than SiBDRV in central North America, Amazon, North Africa, and India.

Figure 11 shows that the ECMWF data assimilation system generally produces stronger surface moisture fluxes than SiBDRV in winter, with a global mean difference of 9.1 W m^{-2}. In summer there are greater differences between SiBDRV and the GCM. The ECMWF data assimilation system gives more latent heat flux than SiBDRV over much of North America, the Amazon region, tropical Africa, and Southeast Asia. The GCM generally produces much more surface latent heat flux than SiBDRV over much of the globe. The seasonal global mean differences of the surface moisture fluxes are 11.9 and 21.3 W m^{-2} for DJF and JJA, respectively.

The partitioning between the surface sensible and latent heat fluxes is largely determined by the ground wetness and vegetation distributions. In the ECMWF model the surface sensible and latent heat fluxes are estimated by the bulk transfer method of *Louis* [1979] and *Louis et al.* [1982]. The latent heat flux was corrected by an efficiency function which depends on soil wetness and the temperature of the surface soil layer. According to *Blondin* [1988] the ECMWF assimilation system tends to overestimate surface evaporation and simulates excessively dry surface soil and excessively cold surface temperatures, especially in the northern hemisphere summer, when compared with surface meteorological observations.

Total surface evaporation in SiB2 is the sum of direct evaporation from interception, soil surface evaporation, and tran-

Figure 9. Net surface net longwave radiation of SiBDRV (top) and comparisons with the ECMWF assimilation system output (middle) and with the GCM simulations (bottom), for DJF and JJA. The contour interval is 10 W m^{-2} in the top panel and 5 W m^{-2} in the bottom two panels.

Latent Heat Flux (W m^{-2})

Figure 11. Surface latent heat flux of SiBDRV (top) and comparisons with the ECMWF assimilation system output (middle) and with the GCM simulations (bottom), for DJF and JJA. The contour interval is 10 W m^{-2} in all panels.

spiration from vegetation, part of the evaporation is regulated by vegetation stomata, which in turn is affected by the root-zone moisture supply and the canopy temperature. The precipitation (Figure 4) is well correlated with the surface moisture flux, indicating that more precipitation generally results in a larger surface latent heat flux.

In the SiBDRV simulation the maximum possible moisture flux from the land surface to the atmosphere is practically determined by the prescribed atmospheric temperature and humidity and the prescribed downward surface shortwave and longwave radiation fluxes. The partitioning between the surface sensible and latent heat fluxes is regulated by the responses of the vegetation to the prescribed precipitation and the ground wetness.

In the GCM simulation, on the other hand, the surface moisture fluxes, the atmospheric temperature and mixing ratio, precipitation, and the soil moisture all interactively feedback on each other. It is not clear which are the forcings and which are the responses. If we assume that the surface turbulent fluxes of heat and moisture are responses to the atmospheric and radiation forcings in the same way as in SiBDRV, then we may interpret the differences of sensible and latent heat fluxes between the GCM and the SiBDRV.
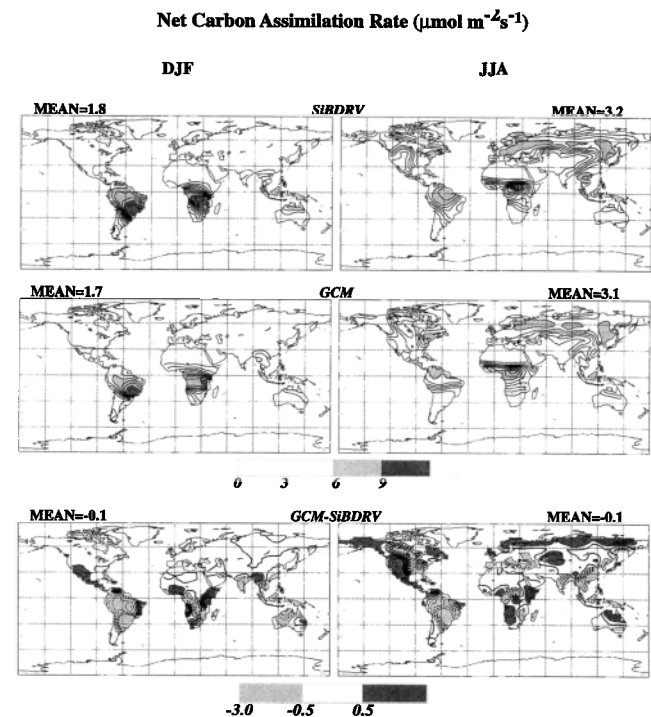
5.4. Carbon Assimilation

Photosynthesis is the only significant mechanism for carbon uptake by the terrestrial biosphere, and it is one of the major sinks for atmospheric CO_2. In Figure 12 we present the simulation results for the canopy net carbon assimilation rate in units of μmol carbon m^{-2} s^{-1} from SiBDRV, and the GCM, and their differences, for DJF and JJA. The net assimilation rate, as represented in SiB2, is total canopy photosynthesis

minus canopy leaf respiration [*Collatz et al.*, 1991; *Sellers et al.*, 1992]. Most of the net carbon assimilation occurs in the tropics, with rates between 6 and 12 μmol carbon m^{-2} s^{-1} throughout the year. The temperate and boreal forests have strong carbon assimilation rates during their growing seasons and show strong seasonal variations. The carbon assimilation rates of the northern temperate and boreal forests are largest during summer and near zero during the winter. Tropical C4 grassland appears to have strong seasonal assimilation changes as well, following the dry and rainy seasons. The maximum assimilation rates for tropical grassland are in DJF, as expected, because that is the wet season for those regions. There is much less seasonal variation in the tropical evergreen forests.

The global mean carbon assimilation rate shows strong seasonal variations too. The seasonal global mean assimilation rate in summer is about twice as large as in winter. This is mainly due to there being more land in the northern hemisphere. SiBDRV and the GCM have similar seasonal variations of the global mean carbon assimilation. The winter global mean assimilation rates are about 56 and 55% of the summer values, for SiBDRV and the GCM, respectively.

Although the seasonality of carbon uptake by vegetation is similar in SiBDRV and the GCM, the relative differences between SiBDRV and the GCM show 10 and 5% more global mean carbon assimilation in SiBDRV than in the GCM, for January and July, respectively. This indicates that the GCM climate generally exerts greater stress on the terrestrial biosphere than the SiBDRV input climate. The major differences are located in the tropical grass land regions in DJF (Figure 12), where there is more precipitation in SiBDRV than in the

Net Carbon Assimilation Rate (μmol m^{-2}s^{-1})

Figure 12. Net carbon assimilation rates simulated in SiBDRV (top) and the GCM (middle) in μmol m^{-2} s^{-1}. The differences between the GCM and the SiBDRV are in the bottom two panels. The contour interval is 1.0 μmol m^{-2} s^{-1} in the top two panels and 0.5 μmol m^{-2} s^{-1} in the bottom panel.

GCM (Figure 4). In summer, much of the net carbon assimilation difference occurs in North America, Southeast Asia and India, and South America because of the precipitation differences, which causes the GCM to impose more soil moisture stress on the vegetation in those regions. The distributions of the carbon uptake differences are significant for the land surface carbon budget and are due to the different climates of SiBDRV and the GCM. The GCM-simulated feedbacks between the terrestrial biosphere and the climate, discussed by *Randall et al.* [1996], may account for the net carbon assimilation differences.

The global total net assimilation rates simulated by SiBDRV and the GCM are shown in Figure 13. The terrestrial biosphere carbon budget includes carbon assimilation by vegetation and respiration by plant leaves, stems and roots, as well as soil respiration. Total carbon uptake by the canopy minus leaf respiration is defined as the gross primary production (GPP) of ecosystem. The GPP minus roots and stem respiration is the net primary production (NPP) of the terrestrial biosphere ecosystem. The global total net carbon assimilation shown in Figure 13 is thus comparable to the GPP if we consider that stem photosynthesis and leaf respiration are very small in comparison with total canopy photosynthesis [*Schlesinger*, 1991]. Estimations of annual mean global GPP over land are 113.4 and 116.6 Gt carbon per year from the GCM and SiBDRV simulations, respectively. It has been estimated that approximately 50 to 60% of the gross carbon assimilation is used for plant respiration [*Schlesinger*, 1991]. Thus the NPP estimates of SiBDRV and the GCM are about 52 and 51 (of 45% GPPs) Gt carbon per year, respectively, which are less than the global mean NPP estimation of 63 Gt carbon per year made by *Leith* [1975] who correlated NPP measurements with local temperature and precipitation. More recent estimates of NPP by *Melillo et al.* [1993] and *Potter et al.* [1993], however, gave 53 and 48 Gt carbon per year respectively, based on comprehensive ecosystem models driven by climate observations and GCM output. Our results illustrate that estimates of global NPP are sensitive to the climate forcing; we see a less estimate of the GPP in the GCM than in SiBDRV, with about 10 and 5% differences of SiBDRV in winter and summer, respectively
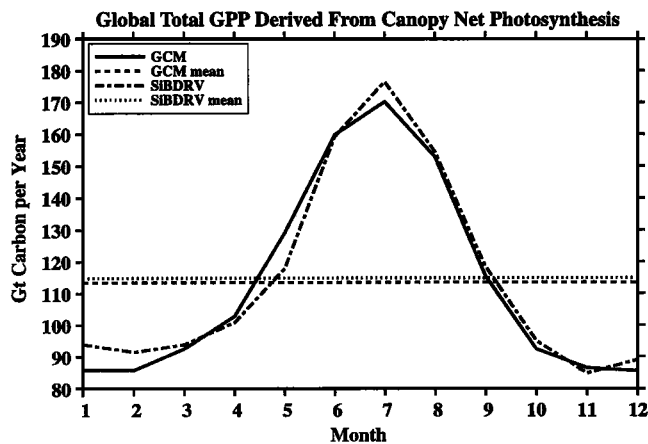
Figure 13. Monthly variations of the gross primary production (GPP) simulated in SiBDRV (dotted-dashed line) and in the GCM (solid line). The annual mean GPP is shown for SiBDRV (dotted line) and the GCM (dashed line). The units are Gt C per year.


Land-Surface CO_2 flux (μmol carbon m^{-2}s^{-1})
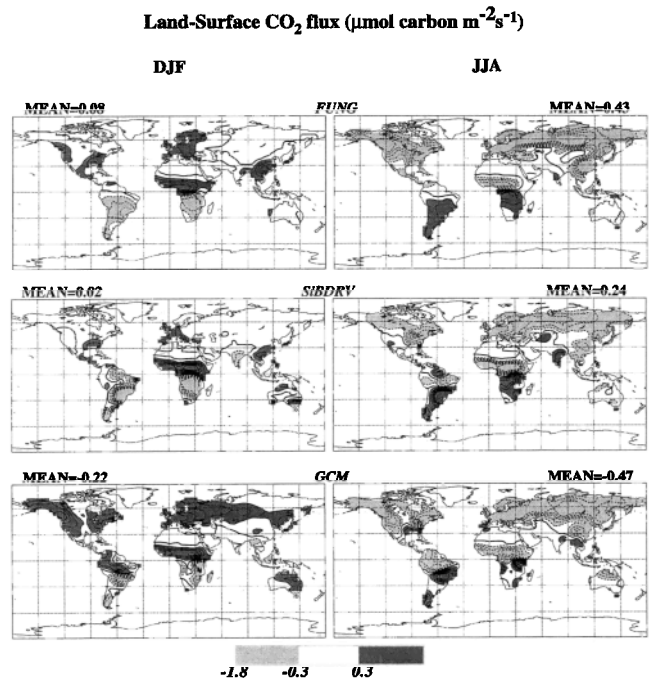
Figure 14. Global distributions of the seasonal mean CO_2 fluxes simulated by *Fung et al.* [1987], in SiBDRV, and in the GCM. The contour interval is 0.3 μmol carbon m^{-2} s^{-1}. The dashed lines indicate carbon uptake by terrestrial biosphere, and the solid lines indicate a net carbon flux into the atmosphere.

(Figure 13). The ratio of NPP to GPP varies among biomes and changes with forest age, so that the 45% NPP to GPP ratio is an estimation of the rule of thumb. The global mean GPP values simulated in the GCM and SiBDRV are reasonably close to other calculations and agree with the total NPP values of 45–65 Gt carbon per year suggested by *Schlesinger* [1991, p. 120].

SiBDRV and the GCM both have maximum global GPP in July and minimum GPP in January (Figure 13) as expected. The SiBDRV GPPs are larger than the GCM estimates for most months, except in April and May. The greatest differences are in winter, indicating that the SiBDRV climate is more hospitable to vegetation than the GCM climate.

Figure 14 shows the distributions of CO_2 fluxes according to *Fung et al.* [1987], and the corresponding results from SiBDRV and the GCM, for DJF and JJA. The CO_2 fluxes for SiBDRV and the GCM are diagnostically calculated under the assumption that annual total carbon uptake by vegetation is balanced by total soil respiration throughout the year, as discussed in section 2.3. In winter the mean CO_2 fluxes between the atmosphere and the terrestrial biosphere are close to zero over much of the land area in high latitudes because of photosynthesis shut-down, frozen soil, and snow accumulation. There are CO_2 releases from soil to atmosphere in western Europe for all three simulations, with a slightly higher CO_2 release over a larger area in the GCM, but less CO_2 release in SiBDRV. Much warmer ground temperatures and lower snow cover (Figure 8) over that region in the GCM, relative to SiBDRV, favors more CO_2 release from the soil in the GCM. During DJF, much of the CO_2 uptake by the terrestrial biosphere is in the southern hemisphere, where photosynthesis

Zonal Total Carbon Flux (10^9 kg carbon yr^{-1} 4-degree-bin^{-1})
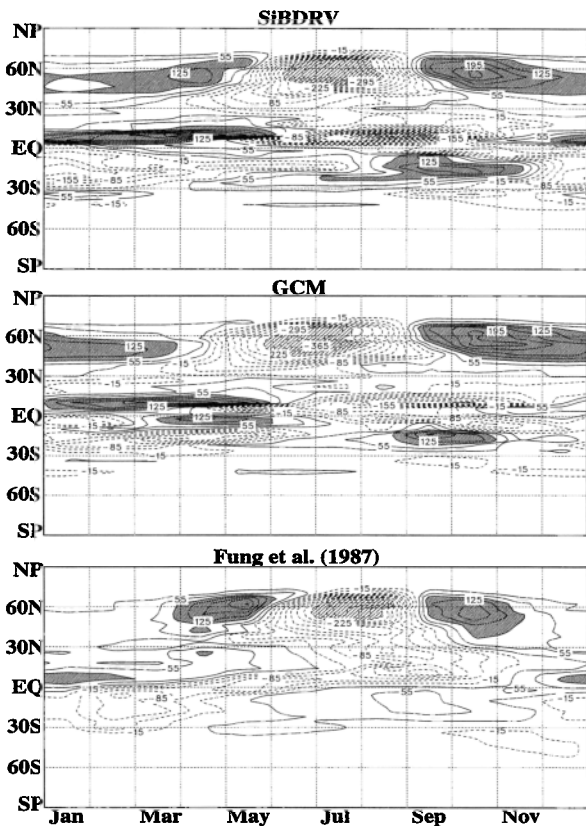
Figure 15. Monthly variations of the zonal total CO_2 fluxes in SiBDRV, the GCM, and *Fung et al.* [1987]. The units are Gt C per year per 4° bin. The contour interval is 35.0 Gt C per year. The dashed lines indicate carbon uptake by terrestrial biosphere, and the solid lines indicate a net carbon flux into the atmosphere.

assimilates more carbon than soil respiration releases. For all of the simulations the strongest CO_2 fluxes are found over the C4 grassland areas of the southern hemisphere. The greatest carbon assimilation occurs here in the GCM and SiBDRV simulations, because for C4 plants, carbon assimilation is more efficient at higher temperatures, compared to C3 plants [*Collatz et al.*, 1991, 1992]. Both the GCM and the SiBDRV show negative carbon fluxes (from atmosphere to biosphere) in India and Southeast Asia, where Fung's calculation shows positive CO_2 release (into the atmosphere) instead. There are differences in the estimates of soil respiration and carbon uptake of the terrestrial biosphere between Fung's method and SiB2. *Fung et al.* [1987] calculated the carbon uptake rate by using the NPP values of vegetation classification weighted by a function of monthly NDVI and the soil respiration rate by the same NPP values weighted by empirical functions depending on climatological surface air temperature. In western North America and the Amazon region the GCM and SiBDRV show significant differences because of their different climates, and especially precipitation (Figure 4).

During JJA, major CO_2 sinks are located in the northern boreal and temperate forests for all three simulations (Figure 14), and CO_2 releases occur over the grasslands in the southern hemisphere. SiBDRV and Fung show net carbon uptake in Southeast Asia, which is contrary to the GCM results. SiBDRV

shows CO_2 release to the atmosphere in western North America, where the summer is dry and warm. Both Fung and the GCM, however, show strong carbon sinks in that region. SiBDRV experiences much less precipitation in western North America (Figure 4) and generally a drier and warmer climate, which often is closer to observations, so that there is much less carbon uptake in SiBDRV than in the GCM (Figure 14).

Figure 15 shows monthly variations of the zonally averaged total CO_2 fluxes between the atmosphere and the terrestrial biosphere, as simulated in SiBDRV and the GCM, and also the CO_2 flux of *Fung et al.* [1987]. Generally, there is good agreement among the three simulations. We see stronger seasonal variations in northern middle and high altitudes as the result of the strong seasonality of the biosphere and strong climate variations during the year. There are weaker seasonal variations in the tropics, but both SiBDRV and the GCM produces stronger seasonal variations than Fung's estimate. In the tropics the carbon assimilation and soil respiration are affected mainly by precipitation, in the wet and dry seasons. In middle and higher latitudes both SiBDRV and the GCM start net carbon uptake earlier than the estimate of *Fung et al.* [1987], between April and May. This earlier CO_2 uptake is supported by the observed decrease of atmospheric CO_2 concentration in the high latitudes in April and May, as discussed by *Randall et al.* [1996].

There are no global CO_2 flux measurements for independent comparison. However, the simulation of atmospheric CO_2 concentration with atmospheric tracer transport models, provided with various surface CO_2 sources and sinks, gives an indirect but independent measure of the CO_2 flux associated with the terrestrial biosphere. *Denning* [1994] simulated the atmospheric CO_2 budget, using the GCM and various prescribed surface CO_2 flux maps. He found that in middle and high latitudes, Fung's land surface CO_2 flux estimate tends to produce too much atmospheric CO_2 in the spring, indicating a too weak CO_2 uptake by the terrestrial biosphere. On the other hand, the SiB2-simulated CO_2 fluxes compared well with observations at the same latitudes.

Although the terrestrial biospheres in SiBDRV and the GCM are represented by the same model, the two coupled systems respond differently to their different climates. There are differences between the soil respiration rates simulated by SiBDRV and the GCM in the middle and high latitudes, where the GCM shows a stronger net carbon release into the atmosphere than SiBDRV between January and March. During spring the GCM starts to produce net carbon uptake at 60°N latitude in April, which is about one month earlier than estimated by Fung. SiBDRV is close to Fung's estimate at that latitude, showing stronger soil respiration in spring. Net carbon uptake begins about 0.5 month earlier than in Fung's results, however.

The major seasonal changes of the CO_2 flux are similar in the GCM, Fung's computations, and SiBDRV, with strong CO_2 uptake in the growing season and soil respiration in spring and fall. The soil respiration continues into the winter season in both the SiBDRV and the GCM, but there is much less soil respiration in Fung's estimate for the same season. This may be due to the fact that the GCM and SiBDRV use the layer-averaged soil temperature to calculate soil respiration, instead of the climatological air temperature used by Fung. In the tropics the GCM and SiBDRV simulate much stronger seasonal changes of CO_2 flux than are found in Fung's estimate. The differences of the tropical CO_2 fluxes are particularly large

in Africa, where the GCM and SiBDRV show more net assimilation in summer (Figure 14). Among the three simulations, SiBDRV shows the strongest seasonal variations in the tropics.

6. Conclusions

The global land surface energy, water, and CO_2 fluxes have been simulated using an off-line land surface process model based on SiB2, using ECMWF data assimilation products to prescribe the atmospheric boundary layer's mean potential temperature, mixing ratio, and wind; ECMWF assimilation system output to prescribe the downward surface solar and thermal radiation; and various observational data sources to prescribe the precipitation and soil and vegetation boundary conditions. The SiBDRV results have been compared with the interactive climate simulations performed with the CSU GCM, with the ECMWF assimilation system output, and with available observations.

The differences between the land surface energy budget components and the surface climatology produced by SiBDRV and the ECMWF assimilation system are due to the differences between the land surface parameterizations used in the two models. The surface net radiation produced by the ECMWF data assimilation system was redistributed and controlled by the soil and vegetation model in SiBDRV, which produced less surface latent heat flux. This is because the large canopy resistent term explicitly formulated by SiB2 and the possible precipitation differences between the SiBDRV precipitation forcing and the ECMWF data. On the other hand, discrepancies between the SiBDRV results and the GCM simulation are related to climate differences, especially differences in incoming solar radiation, precipitation, and snow cover.

The surface flux differences between the ECMWF assimilation system output and the SiBDRV may be affected by inconsistencies in the precipitation forcings seen by SiB2 and the ECMWF land surface parameterization. We are unable to evaluate this effect, however, because the ECMWF precipitation data are not available to us.

The seasonal mean surface-air temperature simulated by SiBDRV is generally cooler than that simulated by the GCM, particularly for DJF. There is more surface net solar radiation in the GCM simulation than in SiBDRV. The GCM tends to have more surface longwave cooling, less surface sensible heat flux, and more latent heat flux. The distributions of the differences in surface sensible and latent heat fluxes are correlated with the precipitation differences.

SiBDRV and the ECMWF assimilation system output are naturally more similar in surface air temperature and water vapor mixing ratio, because the input data for SiBDRV are derived mainly from the ECMWF assimilation system output. The differences between the ECMWF and the SiB2 land surface parameterizations tend to produce different surface energy fluxes, however. The differences between the surface net solar radiation produced by SiBDRV and the ECMWF data assimilation system are due to differences in the land surface albedo, especially due to snow cover effects, vegetation masking, and the snow-free soil albedo. Generally, SiBDRV tends to produce less surface net solar radiation than the ECMWF data assimilation system. There is slightly more surface longwave cooling in the SiBDRV output. SiBDRV tends to reduce the surface latent heat flux and produces more surface sensible heat flux, compared with the ECMWF assimilation system output, particularly in the northern hemisphere summer.

The CO_2 budget of the global land surface has been estimated using SiBDRV and compared with the results of the GCM simulation and with the estimates of *Fung et al.* [1987]. Compared with the GCM, SiBDRV produces about 10 and 5% more global carbon uptake in January and July, respectively, because of climate differences; evidently, the climate produced by the ECMWF data assimilation system is more favorable for plant growth than the GCM's climate. The annual gross primary productions agree well between the SiBDRV and the GCM. Both estimates are well within the range of other studies, using either ecological process models or empirical regression models.

The seasonal CO_2 exchanges between the land surface and the atmosphere were diagnostically estimated for both the SiBDRV and the GCM and agree reasonably well with Fung's calculations. Monthly variations of the zonal total CO_2 flux show that carbon uptake in the boreal and temperate forests in SiBDRV and the GCM occurs about a half month to one month earlier than in Fung's results. There is more soil respiration in the winter months in the GCM, because of the warmer ground. Soil respiration and carbon uptake agree well between SiBDRV and Fung's results for the transition seasons.

Appendix

Equation (4) is similar to the formulation of *Barker et al.* [1994]. For snow-free conditions the land surface albedo was set equal to the ECMWF assimilation system output background soil albedo; that is, $\alpha_{sfcl} = \alpha_{soil}$. The values of the snow water mass per unit area are also taken from the ECMWF assimilation system output. We used a constant ratio of 5 to convert snow water mass into snow depth in meters. In (4), Z_m is defined as the effective snow-masking depth of the vegetation canopy, which corrects for the shading effect of vegetation on snow on the ground and is written as

$$Z_m = Z_1 \frac{\text{LAI}}{\text{LAI}_{max}}. \tag{10}$$

Here LAI is the leaf area index. We use $\text{LAI}_{max} = 1.5$. The ratio $\text{LAI}/\text{LAI}_{max}$ corrects for the canopy leaf shading on ground snow. The SiB2 canopy height Z_1 and seasonal changes of LAI are used in (6). The snow area fraction, according to *Sellers et al.* [1996a], is given by

$$A_s = 13.2, \cdots, \cdot W_{snow}, \qquad 0.0 \le A_s \le 1.0, \tag{11}$$

which is an empirical relationship based on remote sensing data obtained with the scanning multichannel microwave radiometer (SMMR) sensor on Nimbus 7 [*Chang et al.*, 1987, 1990].

The snow surface albedo, α_{snow}, was estimated as the sum of visible snow albedo, α_{snow}^v, and near-infrared snow albedo, α_{snow}^n, weighted by the downward surface visible (S^v) and near-infrared (S^n) radiation fluxes; that is,

$$\alpha_{snow} = \frac{\alpha_{snow}^v \cdot (S^v + 0.5S^n)}{S^v + S^n}, \tag{12}$$

where α_{snow}^v, α_{snow}^n, and the temperature-dependent snowmelting factor F_{melt} are

$$\alpha_{snow}^v = 0.8F_{melt}, \tag{13}$$

$$\alpha_{snow}^n = 0.4F_{melt}, \tag{14}$$

$$F_{melt} = 1. - 0.04 \ (T_g - T_f) \qquad 0.6 \leq F_{melt} \leq 1.0. \quad (15)$$

In (15), T_g is the ground surface temperature and $T_f = 273.16$ K.

References

Barker, H. W., Z. Li, and J.-P. Blanchet, Radiative characteristics of the Canadian climate centre second-generation general circulation model, *J. Clim., 7,* 1070–1091, 1994.

Barkstrom, B. R., The Earth Radiation Budget Experiment (ERBE), *Bull. Am. Meteorol. Soc., 65,* 1170–1185, 1984.

Blondin, C., Research on land surface parameterization schemes at ECMWF, in *ECMWF Workshop Proceedings: Parameterization of Fluxes Over Land Surface,* Eur. Cent. for Medium-Range Weather Forecasts, Reading, England, 1988.

Blondin, C., Parameterization of land-surface processes in numerical weather prediction, in *Land Surface Evaporation: Measurement and Parameterization,* edited by T. J. Shmugge and J. C. Andre, pp. 31–54, Pringer, 1991.

Budyko, M. I., *Heat Balance at the Earth's Surface,* 225 pp., Gidrometeoizdat, St. Petersburg, Russia, 1956.

Burden, R. L., and J. D. Faires (Eds.), *Numerical Analysis* (3rd ed.), pp. 117–135, Prindle, Weber and Schmidt, 1985.

Businger, J. A., J. C. Wyngaard, Y. Izumi, and E. F. Bradley, Flux profile relationships in the atmospheric surface layer, *J. Atmos. Sci., 28,* 181–189, 1971.

Chang, A. T. C., J. L. Foster, and D. K. Hall, Nimbus-7 SMMR derived global snow cover parameters, *Ann. Glaciol., 9,* 39–44, 1987.

Chang, A. T. C., J. L. Foster, and D. K. Hall, Satellite estimates of northern hemisphere snow volume, in *Remote Sensing Letters, Int. J. Remote Sens., 11,* 167–172, 1990.

Collatz, G. J., J. A. Berry, G. D. Farquhar, and J. Pierce, The relationship between the rubisco reaction mechanism and models of leaf photosynthesis, *Plant Cell Environ., 13,* 219–225, 1990.

Collatz, G. J., J. T. Ball, C. Grivet, and J. A. Berry, Physiological and environmental regulation of stomata conductance, photosynthesis and transpiration: A model that includes a laminar boundary layer, *Agric. Forest Meteorol., 54,* 107–136, 1991.

Collatz, G. J., M. Ribas-Carbo, and J. A. Berry, Coupled photosynthesis-stomatal conductance model for leaves of C4 plants, *Aust. J. Plant Physiol., 19,* 519–538, 1992.

Deardorff, J. W., Parameterization of the planetary boundary layer for use in general circulation models, *Mon. Weather Rev., 100,* 93–106, 1972.

Deardorff, J. W., Efficient prediction of ground surface temperature and moisture, with inclusion of a layer of vegetation, *J. Geophys. Res., 83,* 1889–1903, 1978.

Denning, A. S., Investigations of the transport, sources, and sinks of atmospheric CO_2 using a general circulation model, *Pap. 546,* Dep. of Atmos. Sci., Colo. State Univ., Fort Collins, 1994.

Dickinson, R. E., Modeling evapotranspiration for the three-dimensional global climate models, in *Climate Processes and Climate Sensitivity,* vol. 5, edited by J. Maurice Ewing, pp. 58–72, AGU, Washington, D.C., 1984.

Dorman, R. E., and P. J. Sellers, A global climatology of albedo, roughness length and stomatal resistance for atmospheric general circulation models as represented by the simple biosphere model (SiB), *J. Appl. Meteorol., 28,* 833–855, 1989.

European Center for Medium Range Weather Forecasting

(ECMWF), ECMWF data assimilation—Scientific documentation, in *Research Manual Version 2,* edited by Lonnberg and Shaw, 1987.

Fowler, L. D., D. A. Randall, and S. A. Rutledge, Liquid and ice cloud microphysics in the CSU General Circulation Model, 1, Model description and simulated microphysical processes, *J. Clim.,* in press, 1995.

Fung, I. Y., C. J. Tucker, and K. C. Prentice, Application of very high resolution radiometer vegetation index to study atmosphere-biosphere exchange of CO_2, *J. Geophys. Res., 92,* 2999–3015, 1987.

Garratt, J. R., Review of drag coefficients over oceans and continents, *Mon. Weather Rev., 105,* 915–929, 1977.

Goudriaan, J., *Crop Micrometeorology: A Simulation Study,* 249 pp., Wageningen Cent. for Agric. Publ. and Doc., Netherlands, 1977.

Legates, D. R., and C. J. Willmott, Mean seasonal and spatial variability in global surface air temperature, *Theor. Appl. Climatol., 41,* 11–21, 1990a.

Legates, D. R., and C. J. Willmott, Mean seasonal and spatial variability in gauge-corrected global precipitation, *Int. J. Climatol., 10,* 111–127, 1990b.

Leith, H., Modeling the primary productivity of the world, in *Primary Productivity of the Biosphere,* edited by H. Leith and R. H. Whittaker, pp. 237–263, Springer-Verlag, New York, 1975.

Li, Z., and L. Garand, Estimation of surface albedo from space: A parameterization for global application, *J. Geophys. Res., 99,* 8335–8350, 1994.

Louis, J. F., A parametric model of vertical eddy fluxes in the atmosphere, *Boundary Layer Meteorol., 17,* 187–202, 1979.

Louis, J. F., M. Tiedtke, and J. F. Geleyn, A short history of the PBL parameterization at ECMWF, in *ECMWF Workshop on Planetary Boundary Layer Parameterization,* pp. 59–80, Eur. Cent. for Medium-Range Weather Forecasts, Reading, England, 1982.

Melillo, J. M., A. D. McGuire, D. W. Kicklighter, B. Moore III, C. J. Vorosmarty, and A. L. Schloss, Global climate change and terrestrial net primary productivity, *Nature, 363,* 234–240, 1993.

Moats, C. D., C. H. Whitlock, S. R. LeCoy, and C. C. DiPasquale, Satellite estimates of shortwave surface radiation and atmospheric meteorology for the BOREAS experiment region, *NASA Tech. Memo. 109132,* 1994.

Paulson, C. A., The mathematical representation of wind speed and temperature in the unstable atmospheric surface layer, *J. Appl. Meteorol., 9,* 857–861, 1970.

Pitman, A. J., Assessing the sensitivity of a land-surface scheme to the parameter values using a single column model, *J. Clim., 7,* 1856–1869, 1995.

Potter, C. S., J. T. Randerson, C. B. Field, P. A. Matson, P. M. Vitousek, H. A. Mooney, and A. Klooster, Terrestrial ecosystem production: A process-oriented model based on global satellite and surface data, *Global Biogeochem. Cycles, 7,* 811–842, 1993.

Randall, D. A., Harshvardhan, and D. A. Dazlich, Diurnal variability of the hydrologic cycle in a general circulation model, *J. Atmos. Sci., 48,* 40–62, 1991.

Randall, D. A., et al., Intercomparison and interpretation of surface energy fluxes in atmospheric general circulation models, *J. Geophys. Res., 97,* 3711–3724, 1992.

Randall, R. A., et al., A revised land-surface parameterization (SiB2) for GCMs, 3, The Greening of the Colorado State University general circulation model, *J. Clim., 9,* 738–763, 1996.

Sato, N., P. J. Sellers, D. A. Randall, E. K. Schneider, J. Shukla, J. L. Kinter III, Y-T, Hou, and Albertazzi, Effects of implementing the simple biosphere model in a general circulation model, *J. Atmos. Sci., 46,* 2757–2782, 1989.

Schlesinger, W. H., *Biogeochemistry: An analysis of global change,* 108–141, Academic San Diego, Calif., 1991.

Sellers, P. J., Y. Mintz, Y. C. Sud, and A. Dalcher, A simple biosphere model (SiB) for use with general circulation models, *J. Atmos. Sci., 43,* 505–530, 1986.

Sellers, P. J., J. A. Berry, G. J. Collatz, C. B. Field, and F. G. Hall, Canopy reflectance photosynthesis and respiration, III, A reanalysis using enzyme kinetics—electron transport models of leaf physiology, *Remote Sens. Environ., 42,* 187–216, 1992.

Sellers, P. J., D. A. Randall, C. J. Collatz, J. A. Berry, C. B. Field, D. A. Dazlich, C. Zhang, G. Collelo, and L. Bounoua, A revised land-surface parameterization (SiB2) for atmospheric GCMs, 1, Model formulation, *J. Clim., 19,* 676–705, 1996a.

Sellers, P. J., S. O. Los, C. J. Tucker, C. O. Justice, D. A. Dazlich, G. J. Collatz, and D. A. Randall, A revised land-surface parameter-

ization (SiB2) for atmospheric GCMs, 2, The generation of global fields for terrestrial biophysical parameters from the NDVI, *J. Clim.*, *9*, 706–737, 1996b.

Shao, Y., et al., Soil moisture simulation—A report of the Rice and PILPS workshop, in *Project for Intercomparison of Land-Surface Parameterization Schemes (PILPS)*, *IGPO Pub. Ser 14*, December 1994.

Shea, D. J., S. J. Worley, I. R. Stern, and T. J. Hoar, An introduction to atmospheric and oceanographic data, *NCAR Tech. Note*, *NCAR/ TN-404+1A*, Natl. Cent. for Atmos. Res., Boulder, Colo., 1994.

D. A. Dazlich, A. S. Denning, D. A. Randall, and C. Zhang (corresponding author), Department of Atmospheric Science, Colorado State University, Fort Collins, CO 80523-1371. (e-mail: changan@chasm.atmos.colostate.edu)

P. J. Sellers, Laboratory for Atmospheres, NASA GSFC, Greenbelt, MD 20771.